Bridging acquisition and processing: A practical data-driven approach

Nabil Khadiri Yazami[1]*, Van Chuong Do[1], Guillaume Friess[2] and Stéphane Laroche[2] present an efficient and low-impact methodology that delivers data-driven diagnostics to inform both ongoing and future acquisition and imaging strategies.

Introduction

A successful implementation of seismic technologies critically depends on the optimal integration of both mature and emerging technologies in acquisition systems, instrumentation, and imaging methodologies. From an acquisition standpoint, the primary objective is to maximise the informational content of the recorded wavefield by enhancing data quality, increasing signal-to-noise ratios, and accurately capturing the near-surface and subsurface responses of the Earth.

Effective collaboration between acquisition and imaging experts requires a robust data framework to support quantitative analysis and methodological feedback. Ongoing seismic operations provide a valuable context for the acquisition of experimental datasets, provided that such investigations have a negligible impact on production activities. This is typically achieved by temporally constraining test scopes and relying exclusively on existing equipment. To enable this, we have developed an efficient and low-impact methodology that delivers data-driven diagnostics to inform both ongoing and future acquisition and imaging strategies. This approach involves continuously recording repeated shots from a fixed source position across the full active spread, while temporarily suspending all other field operations. This configuration isolates the environmental and subsurface responses, minimising operational interference and enabling a controlled assessment of acquisition performance.

The simplicity, flexibility, and operational compatibility of this procedure allow tests to be implemented at virtually any stage of a seismic survey, regardless of scale or configuration. The resulting experimental datasets provide a rigorous empirical basis for investigating a broad range of acquisition-related questions, including sensor coupling and deployment geometry, source strength and stability, phase and amplitude fidelity, near-surface induced distortions, data robustness in the event of seismic disturbance such as earthquakes, simultaneous-source acquisition feasibility, and the design and validation of source-encoding schemes.

Field experiments

The experimental dataset analysed in this study was acquired over an operational 3D receiver spread consisting of 56 active receiver lines, each 23.6 km in length and spaced 100 m apart (Figure 1). Receiver stations were deployed at 25 m intervals along each line and instrumented with an array of nine 10-Hz geophones (three connected in parallel and three connected in series). For comparative analysis, 16 single-sensor micro-electro-mechanical systems (MEMS) units were deployed along 16 of the receiver lines, each colocated at the barycentre of a geophone array and spaced 100 m apart.

The source consisted of a single 60,000 lb seismic vibrator operating with a customised low-frequency control system. A 12 s force-pilot sweep was employed, covering a frequency bandwidth of 1.5-96 Hz with a flat amplitude spectrum. A low-frequency harmonic distortion reduction algorithm was used to generate a more stable and precise ground force.

A series of repeated sweeps was conducted at a fixed source location. The time interval between successive vibrations was sufficient to avoid residual ground motion interference from previous shots. The sweep repetition strategy was designed to (1) evaluate the accuracy and repeatability of the ground-force signal, (2) identify the record exhibiting the lowest ambient noise level across the active spread for subsequent quantitative analysis, and (3) diversity-stack all repeated records into a single common-shot gather (CSG) with enhanced signal-to-noise ratio, suitable for simultaneous-source simulations.

The complete experiment was executed within approximately three hours. During this period, all production shots and ancillary

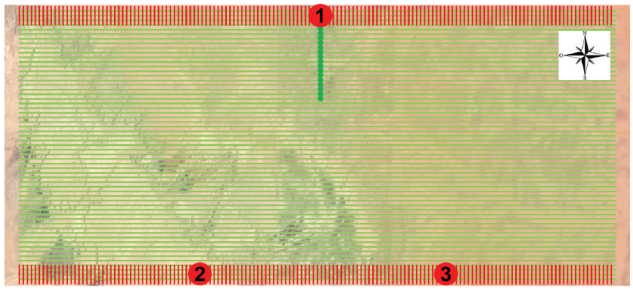


Figure 1 The light-green horizontal lines correspond to the production spread. The red vertical lines correspond to the production sources. The red circles correspond to the repeated source test positions. The dark-green line corresponds to the positions of the MEMS sensors.

[1] Saudi Aramco | [2] Sercel
* Corresponding author, E-mail: nabil.khadiriyazami@aramco.com
DOI: 10.3997/1365-2397.fb2026007

field operations across the spread were temporarily suspended to minimise operational interference and ensure data integrity.

Native data to physical unit conversion

The native field data are recorded in volts for geophone sensors and in pseudo volts for MEMS sensors (Tellier, 2019). To enable a meaningful comparison between datasets acquired using two sensor technologies, arrays of nine planted 10-Hz geophones and a single MEMS node placed on the ground (neither planted nor buried), a conversion is necessary. This step involves converting respective native units to physical quantities such as particle velocity *(m·s⁻¹)* or displacement *(m)*. Moreover, a correction must be applied to account for the frequency-dependent response of the geophones. This pre-processing step has become a prerequisite in the context of full waveform inversion (FWI), which requires both modelled and recorded data to be expressed in consistent physical units. The data correction process is deterministic, being derived directly from the analytical relationships between ground motion and sensor output.

For the geophone, the relationship between the frequency dependent native data $n_G(f)$ and the ground particle velocity $v(f)$ reads:

$$n_G(f) = v(f).G(f; S_G, f_r, \lambda)$$

With $G(f; S_G, f_r, \lambda)$ being the geophone response characterized by its sensitivity (S_G), resonant frequency (f_r) and damping factor (λ)

$$G(f; S_G, f_r, \lambda) = S_G.f^2/(f^2 - 2jf\lambda f_r - f_r^2)$$

For the MEMS, the relationship between the frequency-dependent native data $n_M(f)$ and the ground particle acceleration $a(f)$ reads:

$$n_M(f) = S_Q.a(f)$$

With S_Q being the volt-equivalent sensitivity.

The particle motion expressed in acceleration, velocity or displacement ($d(f)$) is related according to:

$$(j2\pi f)^2.d(f) = (j2\pi f).v(f) = a(f)$$

The MEMS nodes were co-located at the barycentre of each geophone array over 16 aligned cross-line positions (one per receiver line with 100 m spacing between lines). Figure 2 compares the single MEMS data (expressed in $m{\cdot}s^{-1}$) with the geophone array data after vibrator pilot correlation. In Figure 2c, it can be seen that only the unfiltered random noise and air wave (f > 8 Hz) in the MEMS data are visible. The absence of coherent seismic energy in the difference sections validates the correct application of the geophone's inverse and integration (acceleration to velocity domain) filters on the MEMS data. The only remaining differences are attributable to the well-known short-wavelength filtering effect of the field array. The trace-to-trace uncorrelated residuals are naturally removed during stacking processes such as normal move-out stacking and migration. They can also be further attenuated through signal processing techniques designed to remove spatially uncorrelated noise. To compensate for the absence of array-based spatial filtering, it is generally recommended to increase the trace density by increasing receiver and/or source density (carpet shooting concept). The major conclusion drawn from this result is that the seismic signal provided by the acquisition to processing is invariant for the geophone and MEMS sensor.

To go one step further, we also compared the uncorrelated displacement recorded by a geophone array and a single node placed near the vibrators. In this case, the two were not co-located at the array barycentre, but instead positioned at the geophone closest to the source. The purpose of deploying the node near the vibrator was to observe how the low-dwell portion of the

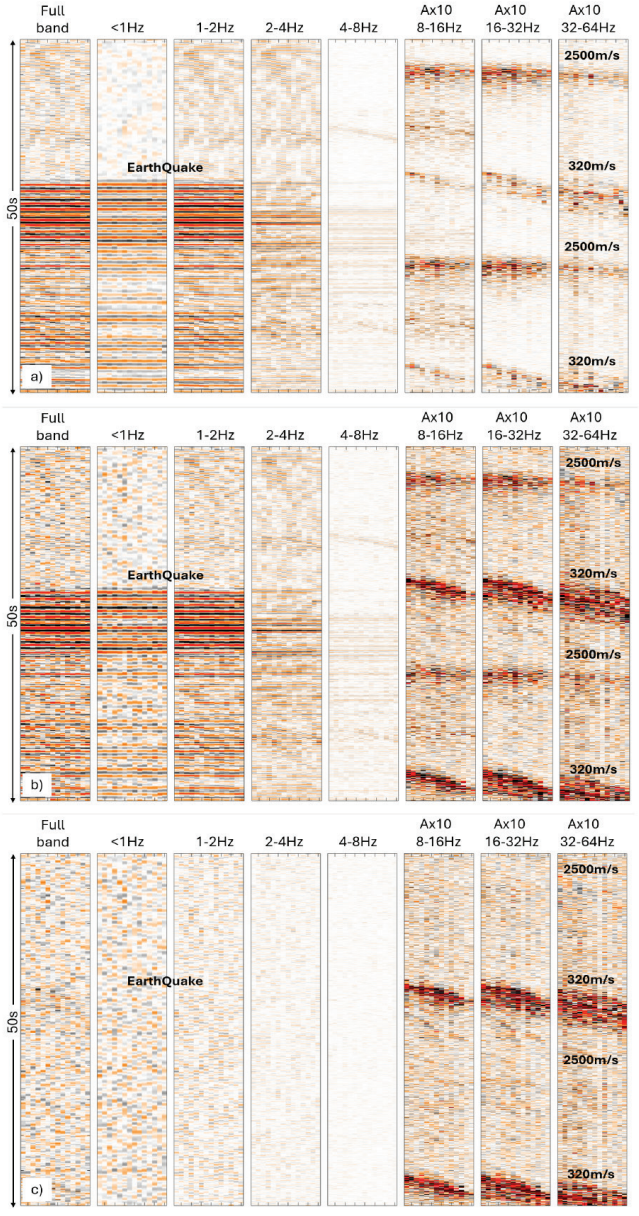


Figure 2 Comparison of the particle velocity field (m·s⁻¹) across 16 sensing positions spaced 100 m apart, for both full-band and sub-band frequency ranges: (a) array of nine planted geophones, (b) single ground-laid MEMS sensor, (c) difference between (b) and (a).

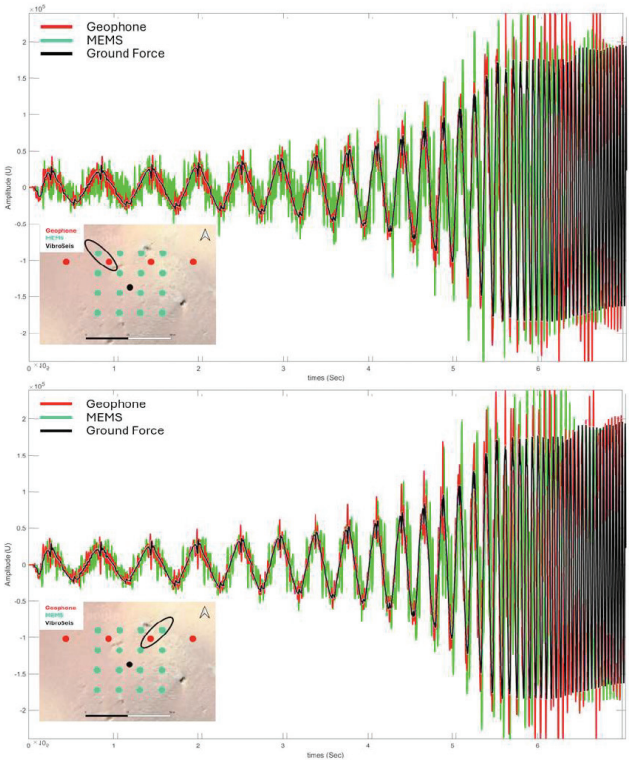


Figure 3 Comparison of the ground force (black curve) with displacements (m) measured by the nearest single MEMS sensor (green curve) and by the geophone array (red curve). A near-perfect correspondence is observed between the displacements recorded by both sensing systems, each accurately reproducing the low dwell-time frequency sweep emitted by the vibrator.

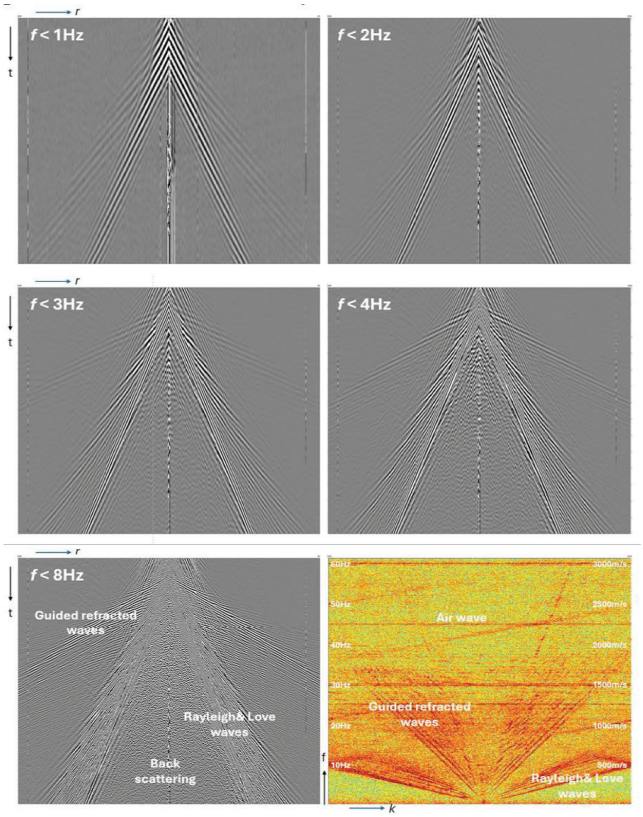


Figure 4 Band-pass filtered CSG along a receiver inline. The wavefield complexity induced by the near-surface signature is illustrated by the presence of multimodal dispersive surface waves and guided refractions.

sweep was recorded by both instruments. Figure 3 shows the relative positions of the geophone array and the MEMS node with respect to the source. A near-perfect phase match can be observed between the array and the single sensor. Both sensors capture the same instantaneous frequency as the ground force. This illustrates the signal equivalence between the geophone array and the ground-laid MEMS sensor for both near-field and far-field measurements.

The near-surface signature

The effect of the near surface in land seismic is often compared to condensation on a window: although only a thin layer, it can significantly blur the image of what lies behind. Here, we confirm that this analogy holds true. The *(x,t)* and *(f,k)* representations of a common shot gather (Figure 4) illustrate how a three-layer near-surface structure with strong velocity contrasts gives rise to complex, multimodal surface waves as well as guided dispersive head waves. These patterns are accurately captured and can be used as input for the simultaneous inversion of both wave types to build a multi-layer near-surface velocity model.

The guided waves formed between the free surface and the high-velocity layer generates multiple reverberations that act as a dephasing and modulation filter on the low-frequency components of the propagating waves, as shown in Figure 5. This observation calls for a proper deconvolution for near-surface effects. At frequencies below 8 Hz, one can clearly observe how backscattering inside the direct ground roll cone masks the

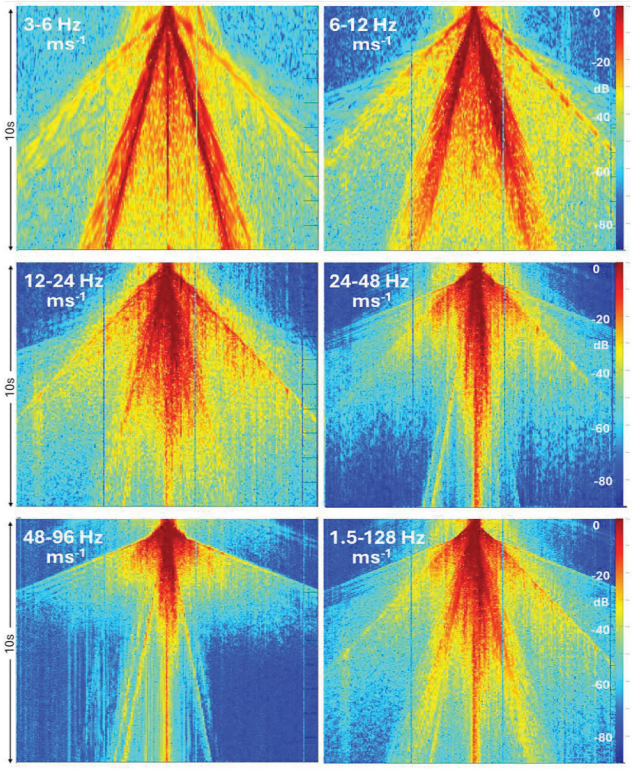


Figure 5 Illustration of the amplitude frequency filtering induced by the near surface.

underlying reflections. The removal of the back scatter apex is best addressed with a multi-azimuth high-density acquisition

geometry which will allow on the processing side to stack out the erratic time of the back scattering while stacking in phase the subsurface-reflected signal. Among all acquisition options, trace density has to be preferred to source intensity.

Active low-frequency emission

The instantaneous force generated by a vibroseis source is frequency-dependent. It starts low at low frequencies, and progressively increases at higher frequencies to reach a maximum peak force. This yields low amplitude output for the low frequency if a constant sweep rate is applied. To compensate for this behaviour, the sweep rate of the pilot can be adjusted according to the vibroseis source's mechanic and hydraulic characteristics as detailed in Tellier et al. (2014). Consequently, a longer emission time is allocated to low frequencies compared to higher frequencies.

Following this approach, we can demonstrate the generation of energetic low-frequency seismic waves across the entire active spread, characterised by a high signal-to-noise ratio (SNR). This is illustrated in *Figure 6*, which presents for five frequencies an overlay of the amplitude and phase rings of the recorded temporal data comprised between 5 s and 7 s after correlation with the pilot sweep. The results highlight the

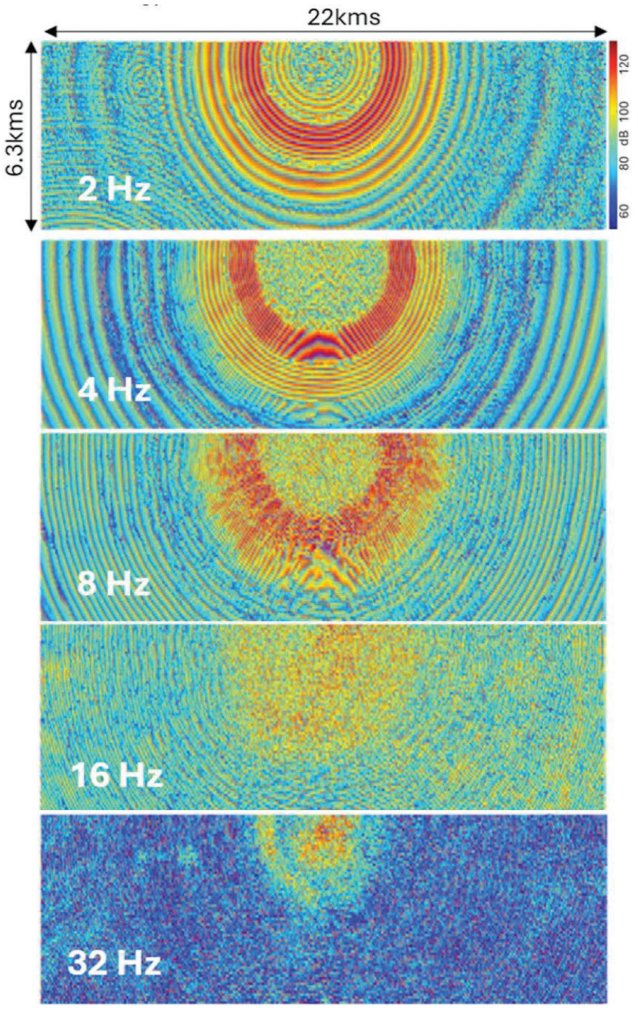


Figure 6 Overlay of amplitude and phase rings for five frequencies over a (5-7s) time window.

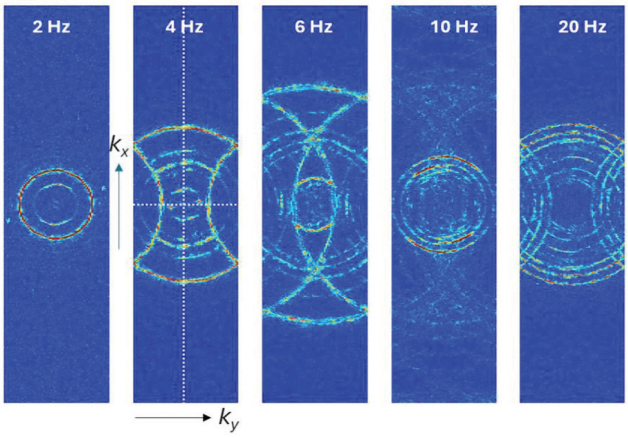


Figure 7 (f, k_x, k_y) amplitude spectra over frequencies 1,4,6,10,20Hz. . $-\frac{\pi}{25m} < \boldsymbol{k_x} \leq \frac{\pi}{25m}; -\frac{\pi}{100m} < \boldsymbol{k_y} \leq \frac{\pi}{100m}$.

spatial radiation of a powerful direct surface-wave wavefront, exhibiting comparable amplitudes at 2 Hz and 8 Hz, thereby confirming the source's effectiveness in generating strong low-frequency energy. The superposition of phase and amplitude rings makes it possible to correlate the amplitude of the various surface-wave modes with their apparent wavelengths which relate to their apparent slowness. The direct ground roll propagates coherently along well-defined rings, followed by a random but still energetic backscattered wavefield. The phase rings associated with the rapidly propagating first arrival head waves also display strong coherence, indicative of a high SNR.

The amplitude spectrum derived from the phase rings displayed in Figure 7 further corroborates these observations. It reveals distinct outer circles corresponding to high-SNR surface waves and inner circles associated with the refracted wavefield, thereby providing additional evidence of the vibroseis source's high efficiency in generating coherent broadband seismic energy.

Simulation of blended acquisition.

To simulate a blended acquisition continuously recorded on a common receiver gather (CRG) with the receiver located at the source position, we applied the reciprocity principle (Source, Receiver) = (Receiver, Source). This approach allows us to interpret a common shot gather (CSG) with a single source and multiple receivers as a CRG recording wavefield generated by multiple shot positions. To reproduce a specific source blending scenario, we generated a long continuous record by summing the unitary traces corresponding to the reciprocal shots, each delayed by a chosen time shift. To minimise the impact of environmental noise, repeated shots at the same position were diversity-stacked and subsequently filtered in the FX domain using the Cadzow algorithm (Trickett, S., 2002, 2003).

The three-step process is illustrated in Figure 8. The main advantage of this physical blending simulation, compared to numerical wave-equation modelling, is that it naturally incorporates real ground conditions, including all the complexities of the near surface. This method is easy to perform, requires minimal time, and can be applied in any

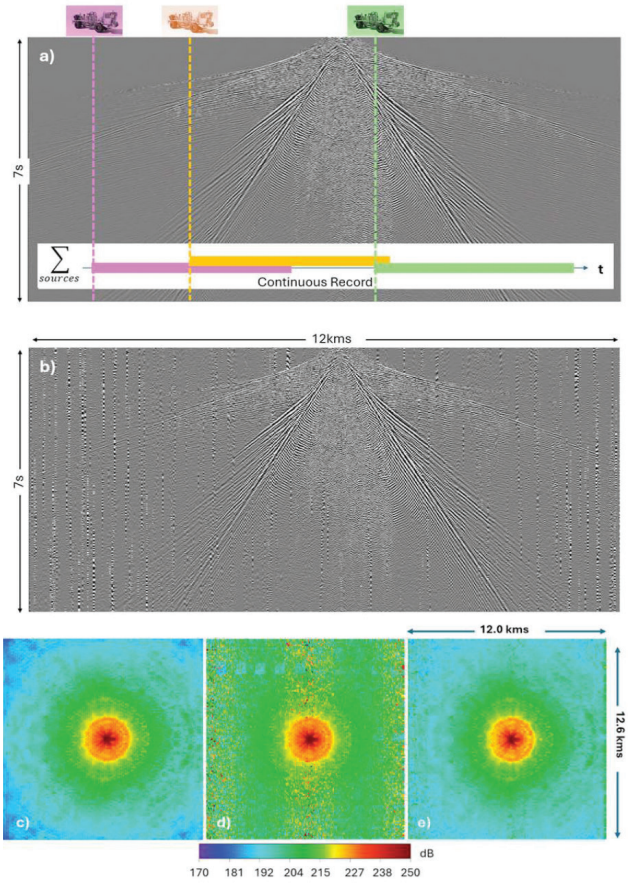


Figure 8 a) CRG derived from field CSG using reciprocity principles. Processing applied: Diversity stack of the 36 shots followed by an FX Cadzow filtering; b) blended continuous record derived from the stack of the individual traces with a delay according to the simultaneous shot scenario. CRG (x, y) RMS amplitude maps over (0-7s) c) before blending d) after a given blending scenario e) after deblending.

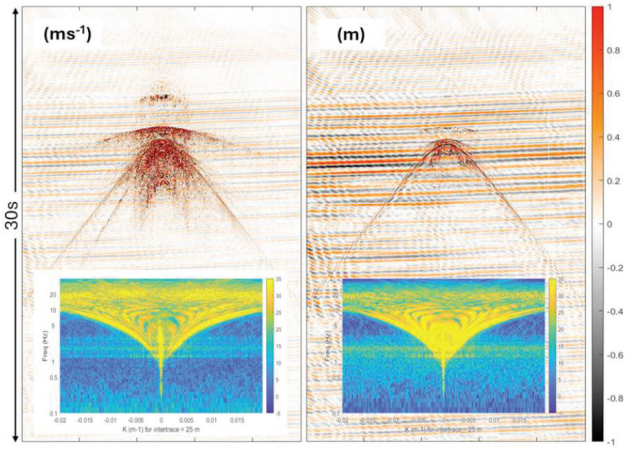


Figure 9 (x,t) and (Log(f), k) of an inline receiver section: velocity (m.s-1, after deconvolution of the geophone response), displacement (time integrated velocity).

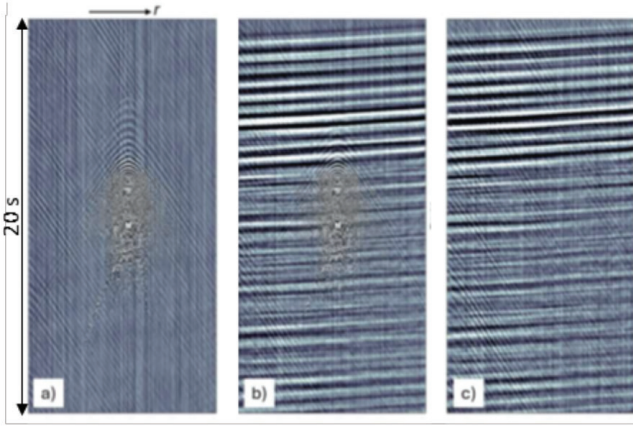


Figure 10 a) CSG before earthquake, b) repeated CSG during earthquake and c) difference.

situation where an active recording spread is available. The results of this simulation enabled the application of an inversion-based deblending for various simultaneous-source scenarios, providing valuable insights into both acquisition-time efficiency and deblending performance (Guillouet et al., 2016).

Passive seismic

Seismic records in the production area are often affected by earthquakes, which manifest as low temporal frequency and low spatial wavenumber waves. These events are clearly visible in the low-frequency region of the spectra of CSGs, or when converted to displacement in the (x,t) domain (Figure 9), the preferred format for vibroseis data processing.

Historically, shot records contaminated by earthquakes had to be reacquired. This required continuous monitoring of seismic activity and real-time communication with the vibrator fleets to halt operations and repeat the shot, a procedure that inevitably impacts productivity. This approach is applicable to both cable-based and nodal acquisition systems.

During our repeat-shot tests, some shots were contaminated by an earthquake. This provided an opportunity to evaluate whether the active seismic signal could be preserved while strong seismological waves crossed the spread. It was verified that the direct difference between an uncontaminated shot and a contaminated shot contained no residual source imprint, leaving only the earthquake records, as if no active seismic source had been activated (Figure 10).

From there, we evaluated the possibility of separating the active and passive wavefield components. Earthquakes are characterised by very long correlation lengths along both the in-line and cross-line directions of the recording spread. This property makes Cadzow-type filtering highly effective (Trickett, S., 2002,2003). Its application on uncorrelated continuous records proved to be particularly advantageous for two reasons: it avoids edge effects associated with data chunking, and it allows greater amplitude focusing on the earthquake signal. These observations indicate that continuous recording mode enables the recovery of active seismic data without the need to re-shoot shots contaminated by earthquakes.

An additional benefit of delivering uncorrelated, continuous field data is illustrated in Figure 11, which presents the recording of very low-frequency surface waves from natural seismicity. These signals provide valuable information for near-surface to deeper characterisation. The integration of passive and active seismic responses, Figure 12, enables the inversion of seismic data across an extended range of temporal frequencies, thereby enhancing the resolution and accuracy of subsurface models.

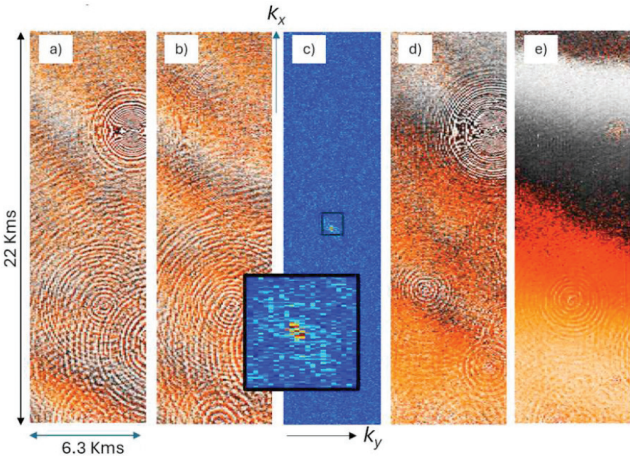


Figure 11 Passive seismicity and earthquake (0.3Hz < f < 0.6Hz). a), b) time slices of ocean wave seismicity, c) associated (f, kx , ky) spectra; d), e) time slices at earthquake time.

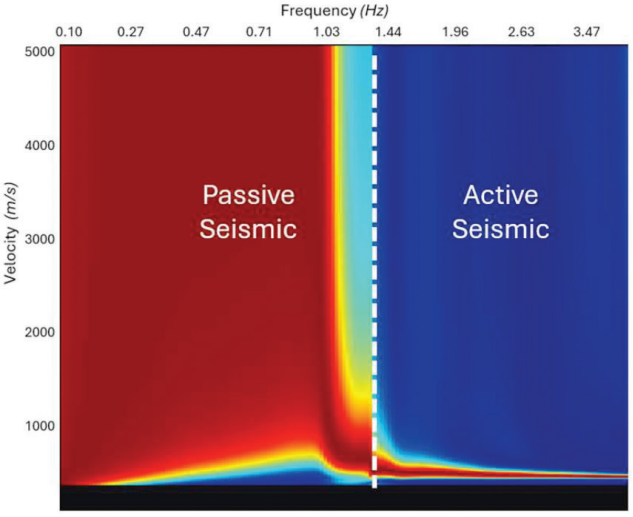


Figure 12 Simultaneous passive and active interferometry for an extended broadband subsurface characterisation.

Conclusion

This study demonstrates the efficacy of a practical, data-driven methodology designed to enhance the integration between seismic acquisition and imaging disciplines. By employing continuous recording of uncorrelated, time-separated repeated shots, we demonstrate that signals acquired from both conventional geophone arrays and ground-laid single MEMS sensors exhibit comparable fidelity and coherence across near- and far-field domains.

The implementation of continuous recording facilitates the robust discrimination between active seismic signals and naturally occurring earthquakes, thereby obviating the need for redundant shot repetitions during seismological events. The high-quality near-surface signature from active seismic and passive ocean wave interferometry captures a complete broadband suite of wave types, enabling inversion for a multilayer near-surface model. Additionally, the quantified backscattering level provides an effective indicator of the trace density required for optimal stacking and coherent noise suppression.

This approach further supports the construction of CRGs for any source code and distance-time activation criteria, to identify the acquisition strategy that minimises residual deblending noise while maximising operational efficiency.

Overall, this operationally flexible and low-impact framework is applicable across multiple stages of seismic surveys and provides a robust foundation for the optimisation of future acquisition and imaging workflows. The findings establish a clear link between acquisition and imaging processes, underscoring the critical role of data-driven methodologies in addressing contemporary challenges in land seismic exploration.

Acknowledgement

The authors acknowledge Stéphane Baris, Raphael Bouvet, Philippe Feugère, Hugo Gomez Ochoa and Philippe Herrmann from Sercel for their contribution to the experiment and for their support during the preparation of this manuscript.

References

Bardainne, T. [2018]. Joint inversion of refracted P-waves, surface waves and reflectivity. 80th EAGE Annual Conference & Exhibition, *Extended Abstracts*.

Boucard, D. and Ollivrin, G. [2010]. Development in vibrator control. *Geophysical Prospecting*, **58**, 3-40.

Guillouet, M., Berthaud, A., Bianchi, T., Pignot, G., Mahrooqi, S. and Shorter, J. [2016]. Recovery of blended data: a sparse coding approach for seismic acquisition. 78th EAGE Annual Conference & Exhibition, *Extended Abstracts*.

Ollivrin, G. and Tellier, N. [2019]. SmartLF for robust and straightforward reduction of low-frequency distortion. 89th SEG Annual Meeting, *Expanded Abstracts*.

Tellier, N. and Lainé, J. [2017]. Understanding MEMS-based digital seismic sensors. *First Break*, **35**(1), 93-100.

Tellier, N.,Ollivrin, G. and Boucard, D. [2014]. Optimising the Generation and QC of Low-Dwell Sweeps. 76th EAGE Annual Conference & Exhibition, *Extended Abstracts*.

Trickett, S. [2002]. F-x eigenimage noise suppression. 72nd SEG Annual International Meeting, *Expanded Abstracts*, 2166–2169.

Trickett, S. [2003]. F-xy eigenimage noise suppression. *Geophysics*, **68**, 751–759.